Multiple relaxation mechanisms in SrBi$_2$Nb$_2$O$_9$ ceramic tweaked by tin and samarium incorporation in assistance with single-step microwave sintering

Anurag Pritam[1,2] · Gourav Bhattacharya[3] · Saurav Sain[1] · Vaibhav Shrivastava[4] · Susanta Sinha Roy[1]

Abstract

Non-stoichiometric lead free polycrystalline Sr$_{0.8}$Sn$_{0.2}$Bi$_{1.75}$Sm$_{0.25}$Nb$_2$O$_9$ (SSBSN) ferroelectric ceramics were synthesized through conventional solid step route method by incorporating ball milling and microwave sintering method. X-ray diffraction along with the Rietveld refinement technique confirms the single-phase orthorhombic structure with A2$_1$ crystal symmetry. Additionally, the short-range ordering was confirmed by Raman spectroscopy. Doping induced crystallite size and strain were further calculated from the Williamson-Hall plot, which comes around 150 nm and 1.48×10^{-3} respectively. A plate like morphology with an average grain size of 0.41 μm was confirmed by scanning electron microscopy (SEM). A diffuse type ferroelectric to paraelectric phase transition was recorded at 395 °C, mostly arising due to structural heterogeneity at the inter-ferroelectric phase boundary. The temperature and frequency-dependent dielectric measurement of SSBSN ceramic reveal a Maxwell–Wagner relaxation, with prominent dielectric loss in a low frequency regime perhaps due to the generation of leakage current in the SSBSN system. Frequency dependent ac conductivity indicates the polaron assisted hopping mechanism in SSBSN, which further obeys Jonscher's formulation. The intra and intergranular contributions to impedance in SSBSN ceramics were probed by the complex impedance spectroscopy (CIS) technique. A non-Debye type relaxation mechanism in SSBSN ceramics was indicated by the Cole–Cole plot, whereas the conduction mechanism and transport properties were briefly studied using modulus spectroscopy.

1 Introduction

Piezoelectric and ferroelectric materials based multifunctional devices have been an indispensable element of our technological evolution due to their comprehensive applications in the electronics, sensors, underwater acoustics, transduces, photorefractive devices, tunable capacitors, pyroelectric sensors, ultrasonic medical imaging and many more. Most of these devices comprise lead-based ferroelectric materials (ex: PZT, PbTiO$_3$) as they possess exceptional ferroelectric, piezoelectric, and pyroelectric properties. However, long-term utilization or exposure to lead can cause serious health issues for humans and the environment due to its toxicity [1, 2]. Thus, from time to time the World Health Organization (WHO) has raised serious concerns regarding the lack of proper disposal of lead and advised material scientists across the globe to search for eco-friendly alternatives [3, 4]. Among all available alternatives the Bismuth layer structured ferroelectrics (BLSF) compositions, have proved to be the most promising ferroelectric system to replace lead based devices in the future due to their exciting properties such as high Curie temperature, high dielectric constant, low polarization switching voltage, good retention behavior, minimum operating voltages, a high mechanical

✉ Anurag Pritam
anurag.pritam64@gmail.com

1 Tyndall National Institute, University College Cork, Cork, Ireland

2 Department of Physics, School of Natural Sciences, Shiv Nadar Institution of Eminence, Greater Noida, India

3 School of Engineering, Ulster University, Newtownabbey, Belfast, Northern Ireland, UK

4 Department of Physics, Shri Khushal Das University, Hanumangarh, Rajasthan 335801, India

quality factor, and large solid solubility of dopant ions, which make them eligible candidates for numerous technological and industrial applications such as satellite communication devices, medical diagnostics, industrial automation, ultrasonic motors, transducers, etc. BLSFs were first discovered by B. Aurivillius in 1949 having a structural formula of $(Bi_2O_2)^{2+} (A_{m-1}B_mO_{3m+1})^{2-}$ where A-site is occupied by mono, dia, and trivalent ion (K^+, Ca^{2+}, Ba^{2+}, Bi^{3+}, etc.) or their combination allowing dodecahedral coordination, B-site is occupied by transitional elements like (Ti^{4+}, Nb^{5+}, Ta^{4+}, Mo^{6+}, etc.) suited to the octahedral coordination and m is an integer which represents the number of BO_6 octahedral layer sandwiched between two perovskite slab [5–8]. Among several BLSFs, the $SrBi_2Nb_2O_9$ (SBN) is the second-layered Aurivillius compound that belongs to the group of disordered uniaxial ferroelectrics with an orthorhombic crystal structure and $A2_1am$ space group. SBN and its solid solution have gained substantial interest due to their less distorted NbO_6 octahedra and extraordinary control of rattling space on the dielectric, ferroelectric, and piezoelectric properties. Despite having numerous useful properties, SBN also suffers from a few drawbacks, such as intense spontaneous polarization and high dielectric loss [9, 10]. Interestingly the electrical and ferroelectric properties of Bi-based SBN strongly depend on the complete or partial site substitution/modification of the parent compound [11]. Therefore, controlling these parameters became extremely important to achieve desired properties for technological applications. According to the available literature, Pritam et al. [12] have reported an enhanced dielectric constant of 120 in Sn doped SBN ($Sr_{0.8}Sn_{0.2}Bi_2Nb_2O_9$) compared to undoped one and serves as a basis of the present work. Additionally, the literature suggests that the dielectric and ferroelectric properties of BLSFs can be strongly enhanced by rare earth substitution such as Sm^{3+}, Ce^{3+}, Nd^{3+}, Pr^{3+}, Gd^{3+}, and Y^{3+} as rare earth elements are known to diminish the generation of mobile oxygen vacancies (arise due to high-temperature sintering) in the solid solution due to their peculiar inimitable electronic structure and lattice distortion [13]. Numerous studies are available on A site, B site, or Bi site modification in SBN, however very few or no reports exist on multiple site modifications in SBN, and its influence on structural, dielectric, and electrical properties in SBN is rarely available [14–16].

Therefore, the present work deals with the investigation of structural contribution to the electrical transport mechanism and multiple relaxation mechanism in $Sr_{0.8}Sn_{0.2}Bi_{1.75}Sm_{0.25}Nb_2O_9$ (SSBSN) ceramics synthesized through green synthesis microwave sintering (MS) method, as MS will drastically reduce the two-step sintering to single step sintering. Several dielectric-derived parameters like Z*, M*, and σ* have been thoroughly investigated to get a complete understanding of the electrical behavior of microwave sintered SSBSN ceramics.

2 Experimental section

2.1 Materials and methods

The polycrystalline $Sr_{0.8}Sn_{0.2}Bi_{1.75}Sm_{0.25}Nb_2O_9$ (SSBSN) ceramics were synthesized using the solid-state route (SSR) method by incorporating single step microwave sintering. SSR is the simplest and most effective way to prepare inorganic bulk compositions. Usually, the SSR method is carried out by intermixing followed by high temperature sintering of a homogeneous mixture of different oxides, nitrates, and carbonates [11, 17]. During the synthesis, numerous parameters like temperature, gas flow, pressure, milling time, etc. can be easily varied to achieve the desired phase and morphology of the composition or its solid solution. Initially, the reagent grade carbonates and oxides of Bi_2O_3 (99.9%), SnO (99.9%), $SrCO_3$ (99.5), Sm_2O_3 (99.9%), and Nb_2O_5 (99.95%), were used as the starting materials. The stoichiometric proportions of starting materials were extensively wet milled for 24 h. in a Retsch PM100 planetary ball mill using hard tungsten carbide balls of diameter 5 mm (the ball to. powder mass ratio was 10:1). The obtained sullery was mixed with the Polyvinyl Acetate (PVA) binder and compressed into a cylindrical pallet having a diameter of 10.8 mm and thickness of 2 mm. Further, the pallets were sintered in a closed crucible at 1000 °C for 5 h. in a microwave furnace having a frequency of 3.5 GHz.

2.2 Characterization techniques

The Phase formation of SSBSN was investigated using Bruker D8 discover equipped with Cu-Kα radiation of wavelength 1.5406 Å, operated at 40 kV and 40 mA. The data was recorded in a step size of 0.02 with a time per step of 2 s for the integrated angular range of 20°–80°. Raman spectra were recorded using a micro-Raman spectrometer equipped with a 532 nm argon-ion laser source with a magnification of 50×. The surface morphology was recorded using Carl Zeiss Merlin VP Compact FE-SEM with 5 kV acceleration voltage and 50 K magnification. The ac conductivity, impedance, and modulus spectroscopy of the prepared composition were calculated using the dielectric data, recorded on high-frequency LCR meter ZM2376 (NF corporation, Japan) with an applied oscillation level voltage of 1 V.
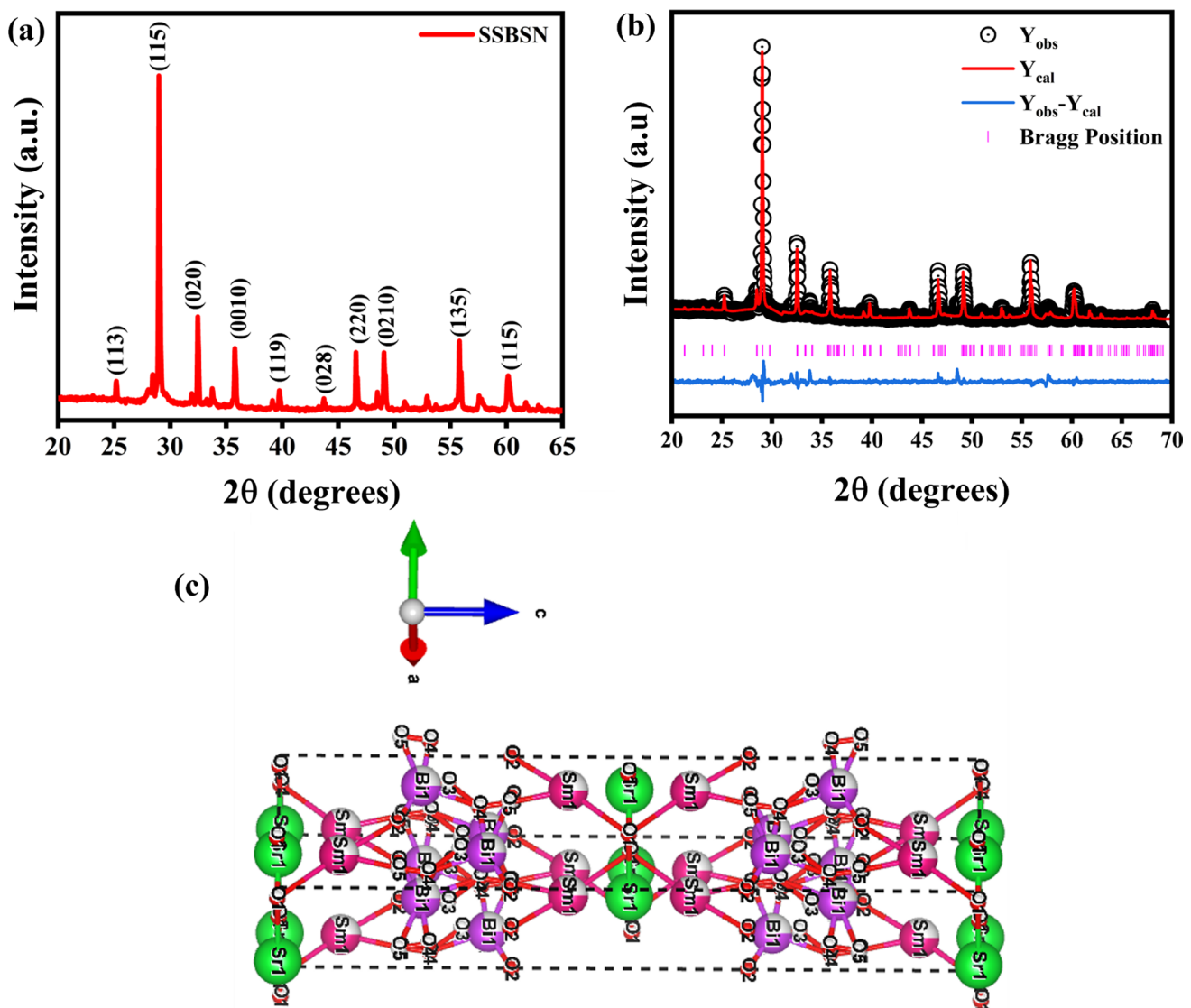
Fig. 1 **a** XRD pattern of microwave sintered SSBSN ceramics, **b** Rietveld refinement profiles of SSBSN ceramic carried out through Full prof software, **c** schematic representation of crystal structure of SSBSN ceramic generated from the refinement parameter

3 Results and discussion

3.1 Microstructural analysis

The X-ray diffraction pattern of Sn and Sm doped SBN ceramics was shown in Fig. 1a, indicating the formation of a perfect layered perovskite phase within the targeted composition. [11, 18]. The obtained diffraction peaks were indexed using orthorhombic symmetry conferring to the JCPDS card no 00-049-0607. The absence of the secondary phase signifies that the Sm and Sn ions have successfully entered their respective sites of the prepared SSBSN solid solution, thus proposing a smooth substitution. Lattice parameters of the prepared composition were found to be. 5.516 Å, 5.503 Å, and 25.038 Å respectively [16,

19]. Further, the XRD pattern of SSBSN was fitted with Rietveld refinement using Fullprof software. The refined XRD pattern is in good agreement with the experimental data having the goodness of fitting around 2.7 as shown in Fig. 1b. The crystallographic findings from the Rietveld refinement are summarized in Table 1, whereas the crystal structure of the same is demonstrated in Fig. 1c.

3.1.1 Crystallite size and the lattice strain estimation

X-ray diffraction is a powerful technique for determining numerous parameters like crystallite size, lattice strain effect, and peak broadening [17, 20–22]. To know the contribution of the factors mentioned above, it is essential to

Table 1 Refined lattice parameters, atomic positions, and profile parameters of SSBSN ceramics

| Parameters	$Sr_{0.8}Sn_{0.2}Bi_{1.75}Sm_{0.25}Nb_2O_9$ (SSBSN)				
Space group	$A2_1am$ (orthorhombic)				
Cell parameters (Å)	a = 5.5070, b = 5.5050, c = 25.0612, $\alpha = \beta = \gamma = 90$				
Unit cell volume (Å³)	759.729				
Density (g/cm³)	7.440				
Chi-square (χ^2)	2.15				
Bragg R-factor (%)	13.6				
R-factors (%)	7.24				
R_p	24.4				
R_{wp}	17.5				
R_{exp}	10.4				
Atomic positions	Elements	X	Y	Z	Occ
	Sr1(4a)	0.07214	0.25527	0	0.39016
	Sn1(4a)	0.07214	0.25527	0	0.3249
	O1 (4a)	0.40206	0.45501	0.00000	0.20066
	Bi1 (8b)	0.55994	0.77341	0.20159	0.5485
	O2 (8b)	0.39939	1.06028	0.31365	1.31651
	O3 (8b)	1.41364	0.79867	0.25270	1.40297
	O4 (8b)	1.06869	0.28527	0.00000	0.38974
	O5 (8b)	1.06442	1.13588	0.83191	0.65914
	Sm1 (8b)	0.58191	0.75021	0.41325	-0.52016
	Nb1 (8b)	1.18647	0.66617	0.38705	1.00495

collect the X-ray diffraction data of standard material and estimate the instrumental broadening using Eq. 1 [23].

$$\beta_d^2 = \left[\beta_{measured} - \beta_{instrumental} \right]^{1/2} \tag{1}$$

Here, β_d is the corrected broadening, $\beta_{measured}$ is measured broadening, and $\beta_{instrumental}$ is instrumental broadening. The physical broadening and instrumental broadening of the sample are estimated by FWHM (Full-width half maxima) [24]. By employing the corrected parameters, the average crystallite size can be determined by Debye Scherrer's equation depicted below.

$$D = \frac{0.9\lambda}{\beta \cos\theta} \tag{2}$$

where D is the crystallite size, λ is the wavelength of X-ray (1.5406 Å), and β is the FWHM [25]. The calculated crystallite size is around 80 nm. Based on Debye Scherer's model, only crystallite size plays a significant role in broadening of XRD peaks, however other factors like lattice strain, also known as strain-induced broadening were neglected. Numerous models, such as the Warren–Averbach method, Williamson Hall (W–H) method, etc., deal with the effect of strain and crystallite size on peak broadening discretely and can
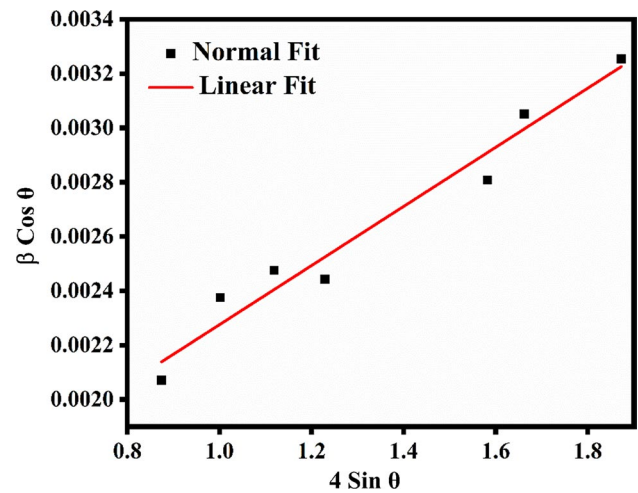
Fig. 2 Williamson–Hall plot of SSBSN ceramics

be employed to estimate the induced strain along with the crystallite size [20, 24, 26]. Among these methods, the W–H method is ideal for this purpose due to its simplified integral breath model, which noticeably differentiates between the crystallite size and strain-driven peak deformation, considering peak broadening as a function of two theta [24, 27, 28]. The total broadening of the diffraction peak is shown below.

$$\beta_{hkl} = \beta_{size} + \beta_{strain} \tag{3}$$

where β_{hkl} denotes the FWHM of a XRD peak, β_{size} and β_{strain} are the widths due to the size and strain, respectively. According to the Uniform Deformation Model (UDM), the strain is isotropic and arises in the crystalline structure due to imperfections, depicted in Eq. 4,

$$\beta_{strain} = 4\varepsilon \tan\theta \tag{4}$$

On rearranging the Eq. 2, 3, and 4, we get

$$\beta_{hkl} = \frac{K\lambda}{D.\cos\theta} + 4\varepsilon.\tan\theta \tag{5}$$

$$\beta_{hkl}\cos\theta = \frac{K\lambda}{D} + 4\varepsilon.\sin\theta \tag{6}$$

Equation 6, known as the uniform deformation model (UDM) equation, reveals the isotropic nature of the crystals. Where D and ε are known as crystallite size and microstrain, respectively [23].

Figure 2 shows the W–H plot of SSBSN ceramics. The calculated value of D and ε comes around 150 nm and 1.48×10^{-3}, respectively. The slope obtained from the W–H plot is found to be in a positive direction, hence generating the intrinsic strain of 1.48×10^{-3} in the system [21, 29].
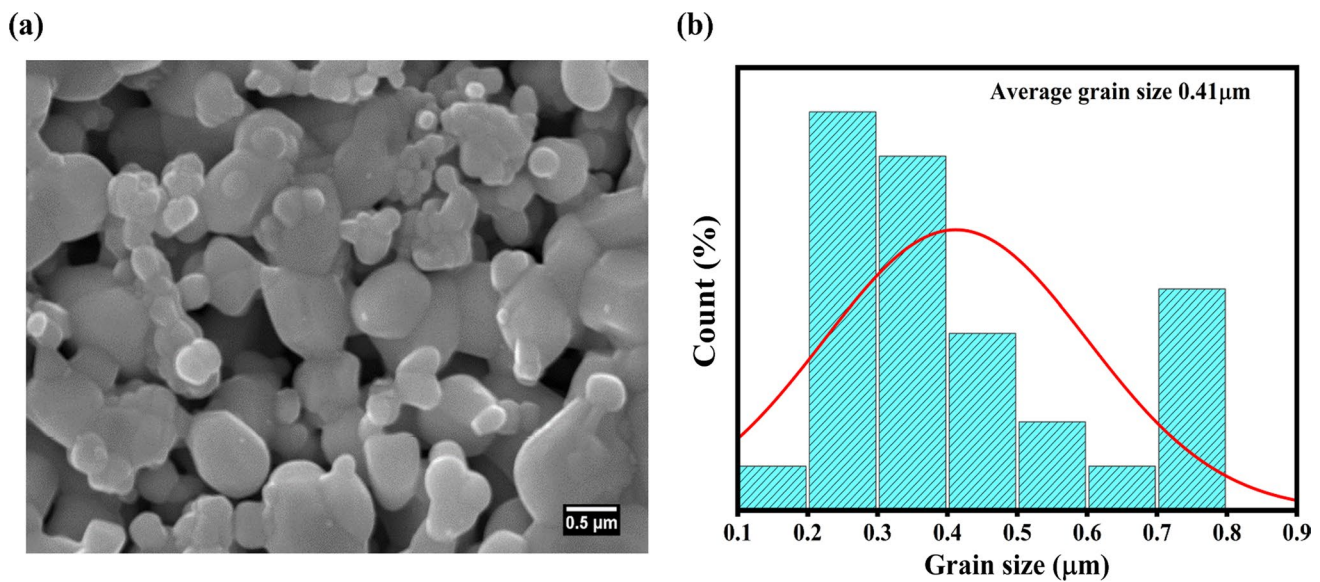
(a)

(b)

Fig. 3 **a** Cross-sectional SEM micrograph, **b** grain size distribution curve of SSBSN ceramics

3.2 Morphological analysis

Figure 3a shows the cross-sectional field-emission scanning electron microscopy (FESEM) micrograph of microwave sintered SSBSN pellet. The SEM micrographs illustrate that the different shapes and sizes of grains have been homogeneously distributed across the surface. The morphology indicates a clear grain boundary with a well-defined compact plate-like structure, which is the signature of the Bismuth layered structured ferroelectrics. Careful investigation of the high-resolution SEM image further indicates the presence of porosity in the composition, mostly arising due to evaporation of Bismuth oxide at high temperatures [30, 31]. The average grain size was calculated using Image J software at a magnification of 50 KX and a scale of 0.5 μm. Normal distribution curve fitting of the histogram was employed to calculate the mean grain size of the composition, which comes around 0.41 μm depicted in Fig. 3b.

3.3 Raman analysis

Raman spectroscopy is a chemical analysis technique, which is used to probe the structural phase transition, crystallinity, lattice symmetry, and polar nanoregions (PNR) linked with the structural disorder of ferroelectric and multiferroic materials [3]. The room temperature Raman spectra of the SSBSN ceramics in a spectral range of 100–900 cm⁻¹ are shown in Fig. 4. A couple of intense peaks with strong Raman intensity were observed at 202.4 cm⁻¹, 570.31 cm⁻¹, and 838.42 cm⁻¹; however, a bunch of weak peaks was also detected at 176.06 cm⁻¹, 270.16 cm⁻¹, 329.27 cm⁻¹, 448.19 cm⁻¹, and 686.04 cm⁻¹ [32, 33]. A sub-intense peak
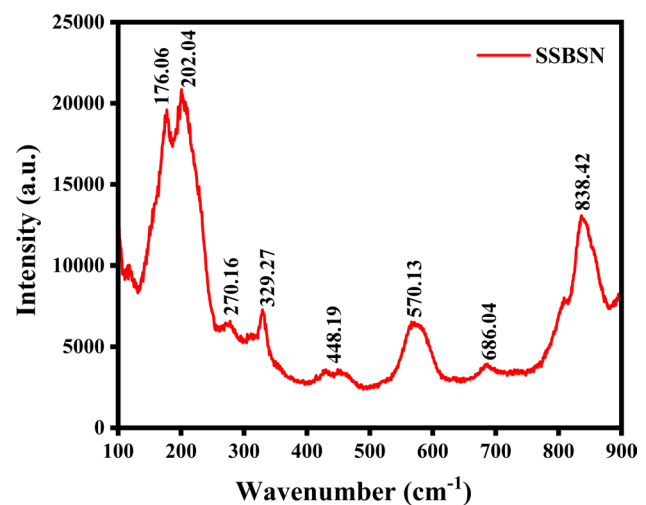

Fig. 4 Room temperature Raman spectra of SSBSN ceramics

was observed at 202 cm-1, which indicates the vibration of A site ions (Sr and Sn) of the pseudoperovskite blocks [34]. Peak located at 570.31 cm⁻¹ harmonizes with rigid sublattice mode and depicts the opposite and equal displacement of positive and negative ions. Raman mode corresponds to 838.42 cm⁻¹ attributed to the symmetric stretching of NbO₆ octahedra, hence implying the supremacy of the orthorhombic phase in the SSBSN system, also confirmed from the XRD analysis of the same. Mode corresponds to 202.4 cm⁻¹ and 686.04 cm⁻¹ assigned to the vibrations of A site ions and asymmetric distortion of BO₃ triangular group and deformation of BO₄ tetrahedron respectively. The Raman mode at 270.16 cm⁻¹ is led by a force constant due to Bi-O₂ and
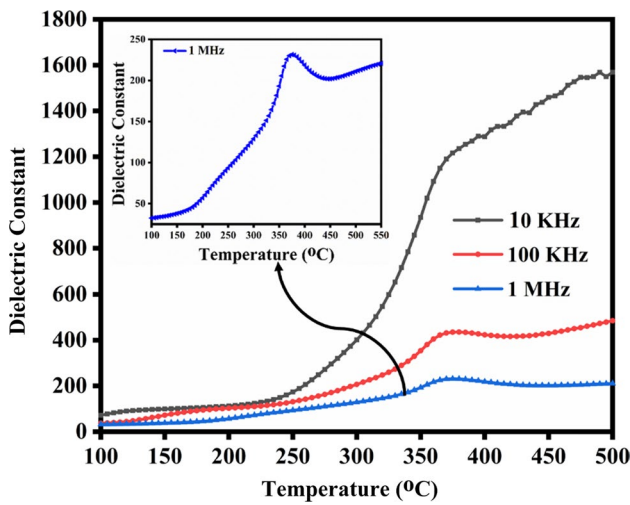
Fig. 5 The dielectric constant of SSBSN ceramics as a function of temperature at variable frequencies 10 kHz, 100 kHz, 1 MHz
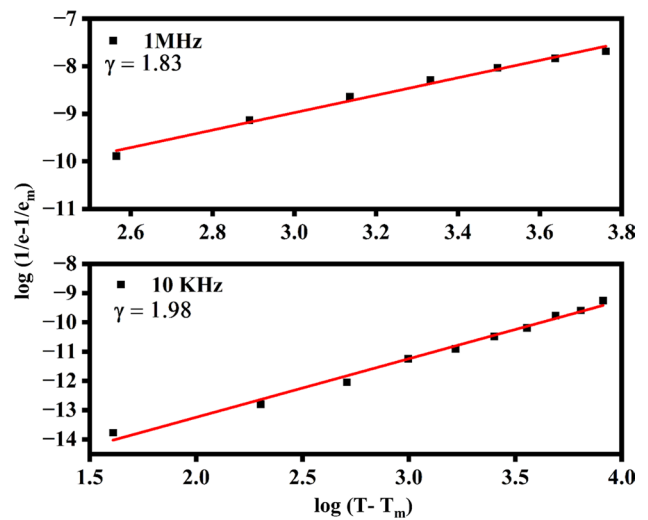

Fig. 6 Plot of $\ln(1/\varepsilon - 1/\varepsilon_m)$ as a function of $\ln(T - T_m)$ at 1 MHz of SSBSN at 1 MHz and 10 kHz (the experimental data are represented by symbols and the solid line represents the fitting of modified Curie Weiss law

Nb-Bi-O_2 bonds. Broad peak arises due to phonon confinement and represents the nanocrystinity of the system [32, 35, 36].

3.4 Curie temperature analysis

Figure 5 illustrates the temperature-dependent dielectric constant of SSBSN ceramics measured at a variable frequency and indicates a clear ferroelectric to paraelectric phase transition at 390 °C. A smaller value of the dielectric constant was observed in the temperature range of 50–250 °C, which linearly increases with the increasing temperature, possibly due to the coupling between mobile charge carriers contributing to the polarization process [37]. A broad peak of dielectric constant was observed for SSBSN ceramics at a frequency of 100 kHz and 1 MHz, arising due to composition fluctuation in solid solution of SSBSN [34, 38–40]. It was reported that defects such as impurities and oxygen vacancies play a significant role in the electronic polarization of BLSFs explaining the nature of dielectric constant at higher temperatures [41].

To determine the diffuseness of a relaxor ferroelectrics, the inverse of dielectric constant and temperature obeys the Uchino and Nomura function, a modified version of Curie–Weiss law (CW) is employed in the present work, shown in Eq. 7 [42]

$$\frac{1}{\varepsilon} - \frac{1}{\varepsilon_m} = \left(T - T_m\right)^{\frac{\gamma}{C}} \tag{7}$$

Here ε_m is the maximum value of dielectric constant at temperature T_m, C is the Curie constant and γ is a degree of diffuseness of phase transition its values range between

1 and 2. $\gamma = 1$ means normal ferroelectrics, whereas $\gamma = 2$ signifies relaxor ferroelectrics respectively [43, 44].

Figure 6 shows the plots of $\log(1/\varepsilon - 1/\varepsilon_m)$ as a function of $\log(T - T_m)$ of SSBSN ceramics. For both measurements, the value of γ is 1.83 and 1.98 respectively, which indicates the diffuse phase transition in SSBSN ceramics, arises due to the formation of mobile oxygen vacancies in the solid solution [2, 45].

3.5 Variation of dielectric constant and loss with frequency

Investigating the temperature and frequency dependent dielectric properties is necessary to understand the conduction mechanism, and relaxation process in solids [46]. In this regard, the frequency-dependent variation of real part of the dielectric constant of SSBSN ceramics at several temperatures is shown in Fig. 7a.

A strong dispersion behavior was observed at low frequency region, possibly due to the accumulation of space charge in SSBSN solid solution. Such resilient dispersion behavior of dielectric constant emerges to be a common feature in ferroelectrics associated with non-negligible ionic conductivity, also known as low-frequency dielectric dispersion (LFDD) [47–49]. A high dielectric constant was witnessed at low frequency, irrespective of temperature, possibly due to the contribution from all four types of polarization electronic, ionic, orientational, and space charge polarization to the total dielectric constant. A steady decrease in dielectric constant was observed and can be explained by Koop's theory and Maxwell–Wagner model [50]. The tanδ
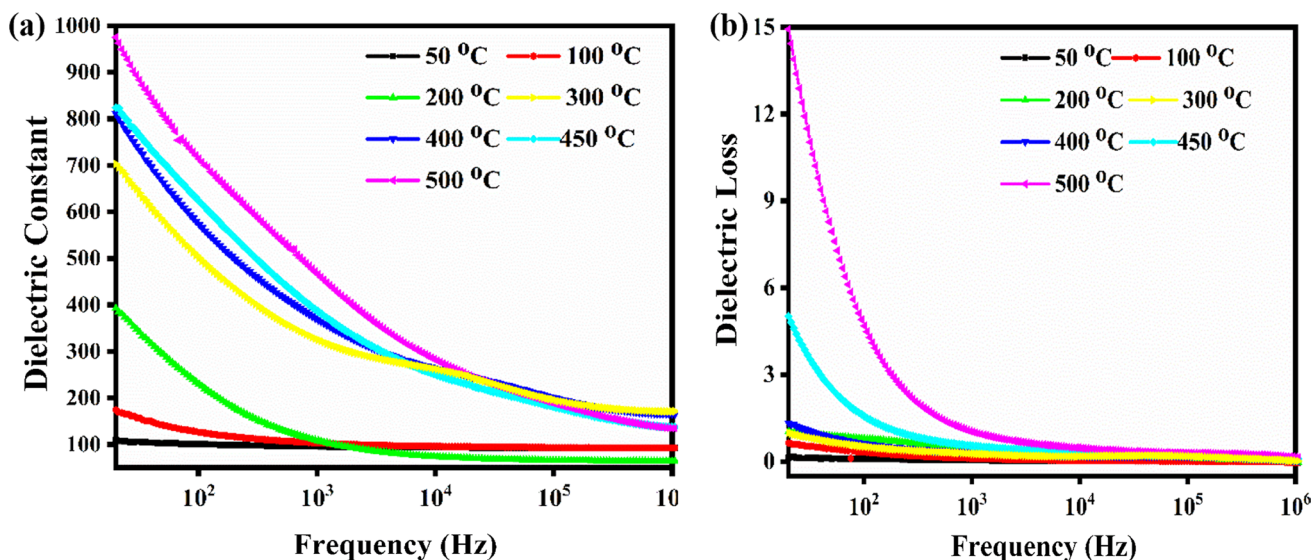
Fig. 7 Variation of **a** dielectric constant and **b** dielectric loss as a function of frequency at different temperatures

or dielectric loss is the energy utilized in rotating the atomic dipole in a dielectric material and it arises due to two major reasons domain wall motion under the influence of external applied field and space charge relaxation. Further, it depends on three parameters frequency, temperature, and nature of additives [51]. Figure 7b shows the frequency dependence of dielectric loss at different temperatures, a high loss was observed in low frequency regions, possibly due to the presence of space charge polarization, however, it drastically decreases at high frequency regions, thus endorsing the surge of domain wall motion in this region [12].

3.6 Ac conductivity analysis

To investigate the conduction process and polaron responsible for the conduction, the temperature dependent a.c conductivity as a function of frequency was studied for SSBSN ceramics, which was calculated using Eq. 8.

$$\text{a.c. Conductivity } (\sigma_{ac}) = 2\pi f \varepsilon_0 \varepsilon' \tan \delta, \tag{8}$$

where f is frequency, ε_o and is permittivity in a vacuum, ε' is the permittivity of the medium, and tanδ is known as dielectric loss[52].
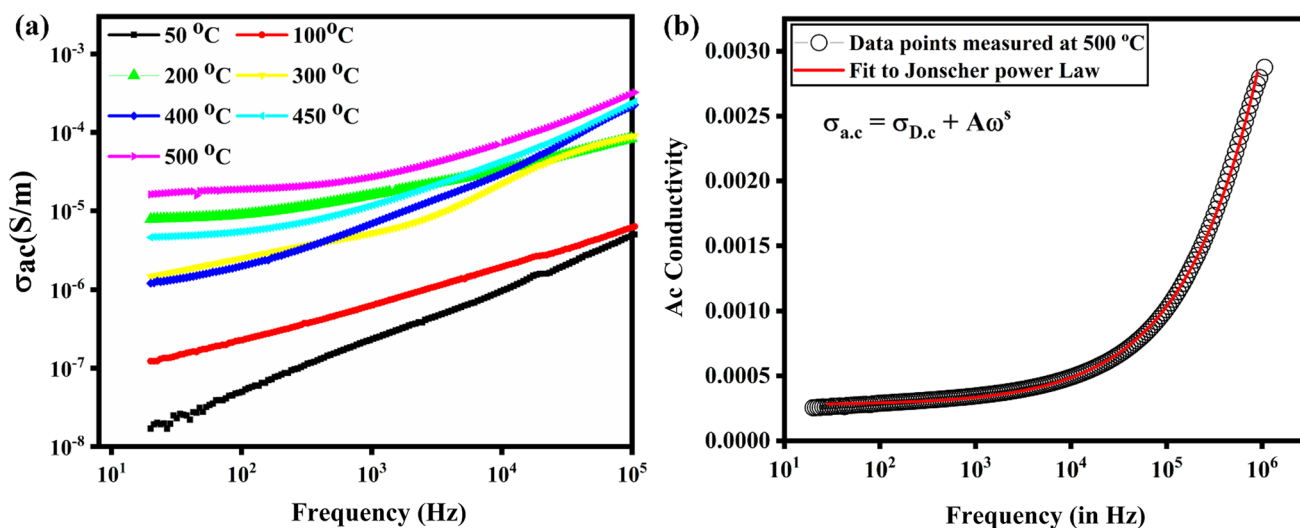

Fig. 8 **a** Variation of ac conductivity versus frequency at several temperatures, **b** fitting of Jonsher's power law to the experimental data of SSBSN at 500 °C

Figure 8a depicts the variation of ac conductivity as a function of frequency, the conductivity curve can be widely differentiated into three regions; the first is low-frequency regions, in this region, the ac conductivity is independent of frequency and decreases with the decrease in frequency. This decrease in conductivity corresponds to the variation of space-charge polarization at the electrode interface and generation of oxygen vacancies in the system. Here local electric field opposes the applied electric field and limits the conductivity. As we increase the frequency, a flat plateau-like region is spotted, where conductivity is independent of frequency, representing the system's dc conductivity (σ_{dc}). The third and final region, known as the high-frequency region, which usually demonstrates the dispersive behavior of conductivity, appears due to the short and long polaron hopping in the SSBSN system. The increasing trend of ac conductivity might be due to the anarchizing of cations among the neighboring sites [53]. One can notice that the nature of the curve is independent of temperature; however, the onset of the dispersion is shifted to a higher frequency as the temperature is further increased. Additionally, the behavior of a.c. conduction was examined by Jonsher's power law shown in Eq. 9.

$$\sigma_{a.c} = \sigma_{dc} + A\omega^s, \tag{9}$$

where A is a temperature-dependent parameter and s is a dimensionless exponent that describes the degree of interaction, whose value lies between 0 to 1, which represents the resistive and capacitive behavior of a material, respectively. The calculated value of s for SSBSN ceramics is shown in Table 2 and reveals a non-Debye type conduction mechanism.

3.7 Complex Impedance Spectroscopy

Complex impedance spectroscopy (CIS) is a powerful tool to probe the dielectric material, which tells us about the individual contribution of different electrical active regions. Usually, CIS is utilized to investigate the microscopic and macroscopic properties of the material like charge transfer resistance, diffusion process, relaxation process, transport number, etc. [54]. The complex impedance is depicted in Eq. 10.

$$\mathbf{Z}* = -i\omega C_o \varepsilon *. \tag{10}$$

Z* is further resolved in real (Z′) and imaginary part (Z″) of impedance and shown below.

$$Z' = \frac{1}{2\pi f C_o}\left[\frac{\varepsilon''}{\varepsilon^2 + \varepsilon''^2}\right] \tag{11}$$

$$Z'' = \frac{1}{2\pi f C_o}\left[\frac{\varepsilon'}{\varepsilon'^2 + \varepsilon''^2}\right] \tag{12}$$

where f is frequency, ε' and ε'' are real and imaginary parts of the dielectric constant, and C_o is known as the capacitance of vacuum[10, 55].

Figure 9a shows the variation of the real part (Z′) of impedance as a function of frequency in a temperature range of 350–550 °C. It was observed that the value of Z′ shows higher values at low-frequency regions, which drastically decreases with increasing frequency till 1 kHz. Beyond that, an independent behavior of the Z′ was observed which eventually merges at high frequency and indicates a release of space charge from the system. The value of Z′ significantly decreases with increasing temperature and indicates the negative temperature coefficients of resistance (NTCR) behavior [47, 48, 56]. Figure 9b shows the variation of the imaginary part of impedance (Z″) with frequency at different temperatures. An asymmetric broadening of the peak was observed with increasing temperature (beyond 405 °C) which indicates multiple relaxations process in the SSBSN ceramics. With the increasing frequency and temperature, the magnitude of Z″ peak was found to shift towards the high-frequency region, indicating that the relaxation mechanism spread over a wide range of frequencies. Irrespective of temperatures, the Z″ attains a constant value beyond 10 kHz, which indicates thermally driven relaxation mechanism in SSBSN ceramics [46, 47, 57].

The Cole–Cole plot of SSBSN ceramics at different temperatures is shown in Fig. 10. A linear response was observed at a lower temperature (> 400 °C) and implies the insulating behavior of the sample. As the temperature rises above 400 °C, the linear response was found to deviate into a semicircular one, indicating the rise of the conductivity in the material. Each semicircle experiences a small divergence from the origin and depicts non-Debye type relaxation process. This type of behavior in Cole–Cole plot arises due to numerous contributing factors such as grain boundary contribution, stress–strain phenomena, atomic and ionic defects distribution, etc. The emergence of two semicircles was also observed at higher temperatures, revealing that the contribution was from both grain and grain boundaries [12, 31, 53, 58]. The lack of a third semicircle rules out the interfacial contribution to total impedance of the system.

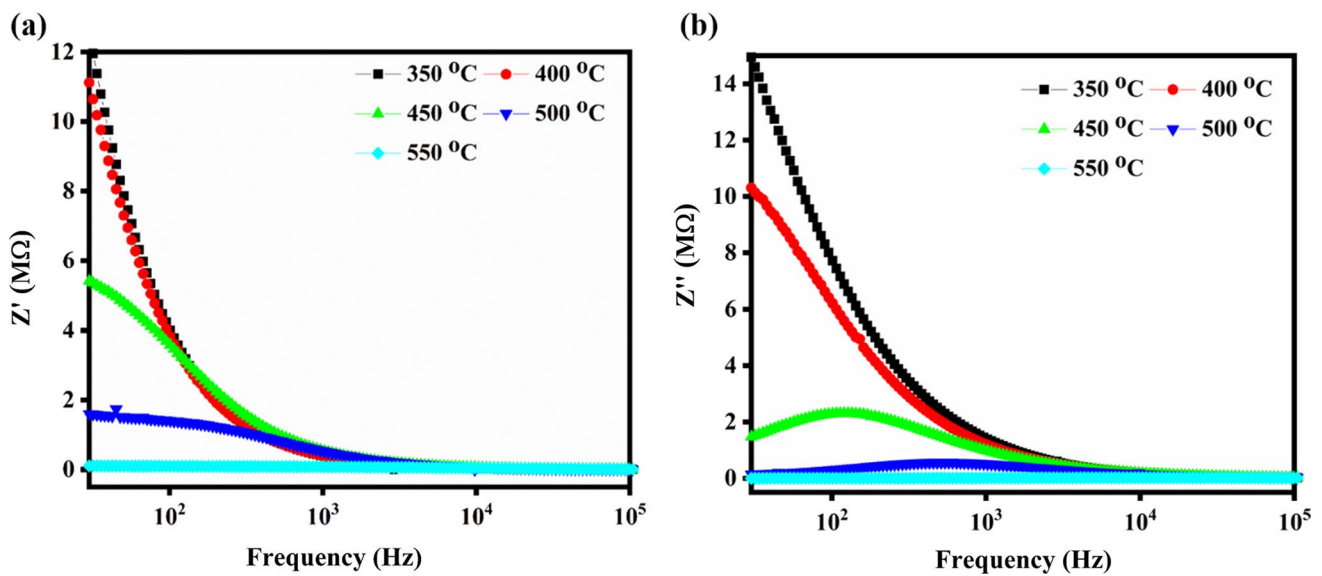| **Table 2** Variation of 's' with temperature of microwave sintered SSBSN ceramics	Temp. (°C)	50	100	200	300	400	450	500
	s	0.625	0.451	0.286	0.469	0.626	0.529	0.407

Fig. 9 Variation of **a** real and **b** imaginary part of impedance as a function of frequency at different temperature
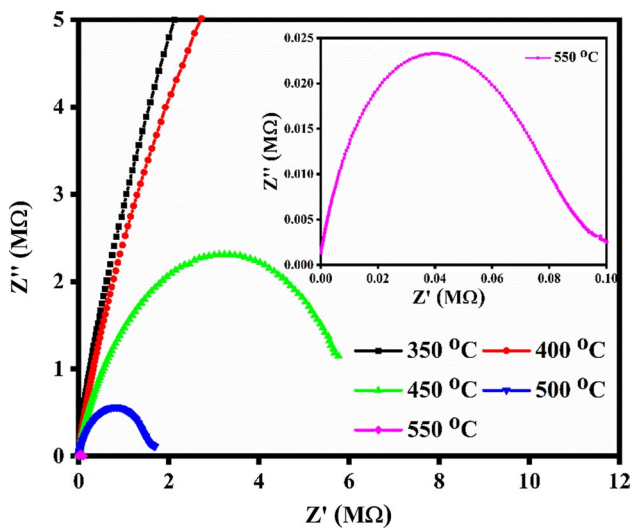

Fig. 10 Cole–Cole plot of microwave sintered SSBSN ceramics at different temperatures

3.8 Complex modulus spectroscopy (CMS)

Unlike the resistive part, the capacitive element also significantly contributes to the impedance spectra of the material. Thus, it might be possible that the researcher can observe a single semicircle in a CIS but can observe multiple peaks in the modulus plot. Thus, to precisely know the contribution of resistive or capacitive components, we must need to investigate our data for the complex modulus spectroscopy (CMS). CMS is a convenient technique to examine the transport properties of dynamical systems[59]. Mathematically CMS is depicted in Eq. 13[55, 60]

$$\mathbf{M}^* = \frac{1}{i\omega C_o Z^*} \tag{13}$$

M* can be further resolved into real (M′) and imaginary component (M″)

$$\mathbf{M'} = \frac{\varepsilon'}{\varepsilon'^2 + \varepsilon''^2}, \ \mathbf{M''} = \frac{\varepsilon''}{\varepsilon'^2 + \varepsilon''^2} \tag{14}$$

Figure 11a illustrates the frequency dependent variation of the real component of modulus at some selected temperatures. It was observed that M′ achieves a constant value above 1 kHz, but approaches zero at the lower frequency region, thus confirming the existence of interfacial or atomic polarization in the SSBSN solid solution. A strong dispersion behavior is observed at the high-frequency region irrespective of temperature, which contributes to the conduction phenomena that arise due to the movement of the charge carrier under the action of an applied electric field in the studied temperature region [55, 61]. A shift in the dispersion region is also observed at high temperatures and supports the long-range mobility of the charge carrier. Figure 11b shows the variation of the imaginary part of the modulus of SSBSN ceramics at several temperatures, a substantial shift in the peak of M″ observed with increasing temperature, indicating a thermally driven relaxation process in solid solution [62]. A nonsymmetrical broad peak is perceived for all measurements, which demonstrates multiple relaxation processes in SSBSN ceramics with different time constants. Finally, a decrease in the magnitude of M″ peak is detected with the increasing temperature, which undoubtedly specifies the surge in the dielectric constant of the SSBSN ceramics [19, 31, 63].
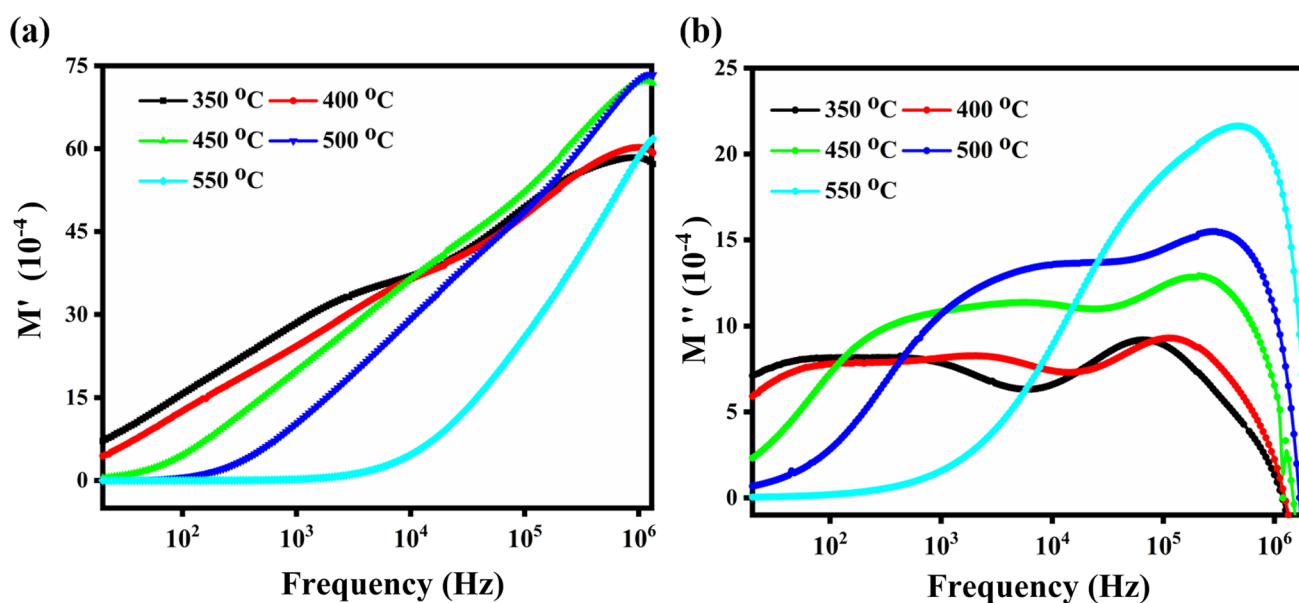
(a)

(b)

Fig. 11 Variation of **a** real and **b** imaginary part of complex modulus as a function of frequency at variable temperature

4 Conclusion

In summary, we have successfully prepared novel $Sr_{0.8}Sn_{0.2}Bi_{1.75}Sm_{0.25}Nb_2O_9$ (SSBSN) ferroelectric ceramics through single step solid state route method by incorporating microwave sintering technique, which drastically reduced the processing parameters (temperature and time) of SSBSN ceramics. XRD and Raman spectra validate the defect free orthorhombic crystal structure with $A2_1am$ space group. Additionally, the Rietveld refinement and Williamson Hall method were used to calculate lattice parameters, atomic position, and strain in SSBSN matrix. A plate like morphology with an average grain size of 0.41 μm was confirmed by scanning electron microscopy (SEM). Temperature dependent dielectric measurement (Tc) indicates diffuse type phase transition, which arises due to the presence of an interacting ferroelectric cluster on the SSBSN. Further, the degree of diffusiveness (γ) was checked by Uchino and Nomura function, which comes around 1.8. Impedance analysis depicts the non-Debye type conduction mechanism with the NTCR behavior, whereas grain, and grain boundary contribution was revealed by Cole Plot. Modulus spectroscopy indicates that the relaxation process in SSBSN was governed by hopping of mobile oxygen vacancies. Ffrequency dependent AC conductivity demonstrates the dispersive behavior of conductivity, arising due to the polaron hopping in the SSBSN matrix. The obtained results support that the SSBSN can be used as a potential candidate for high frequency power transformer applications.

Declarations

Conflict of interest The authors declare that there is no conflict of interest or any personal relationship that could have influenced the work reported in this paper.

Ethical approval This work does not deal with any experiment regarding embryo and human tissue.

References

1. V.K. Sharma, R. Nathawat, S.S. Rathore, Dielectric properties correlation with microstructure in ABi4Ti4O15 (A = Sr, Ba) bismuth layered ferroelectrics. Mater. Adv. **3**, 4890–4898 (2022). https://doi.org/10.1039/d2ma00333c

2. Z. Zhou, X. Dong, S. Huang, H. Yan, Dielectric relaxation of La3+-modified Bi3TiNbO 9 aurivillius phase ceramics. J. Am. Ceram. Soc. **89**, 2939–2942 (2006). https://doi.org/10.1111/j.1551-2916.2006.01166.x

3. S. Sahoo, D.K. Pradhan, S. Kumari et al., Structural heterogeneity induced enhancement of physical properties in Sm-modified K0.5Na0.5NbO3. J. Am. Ceram. Soc. (2023). https://doi.org/10.1111/jace.19612

4. A.F. Lima, Optical properties, energy band gap and the charge carriers' effective masses of the R3c BiFeO3 magnetoelectric compound. J. Phys. Chem. Solids (2020). https://doi.org/10.1016/j.jpcs.2020.109484

5. P. Fang, H. Fan, Z. Xi et al., Structure and electrical properties of bismuth and sodium modified SrBi2Nb2O9 ferroelectric ceramics. J. Alloys Compd. **550**, 335–338 (2013). https://doi.org/10.1016/j.jallcom.2012.10.147

6. S. Inai, J. Sato, R. Aoyagi et al., Piezoelectric properties of V and Ba substituted SrBi2 Nb 2O9 ceramics. Ferroelectrics **358**, 148–152 (2007). https://doi.org/10.1080/00150190701537109

7. Z. Tang, J. Chen, B. Yang, S. Zhao, Energy storage performances regulated by layer selection engineering for doping in multilayered perovskite relaxor ferroelectric films. Appl. Phys. Lett. (2019). https://doi.org/10.1063/1.5087045

8. S. Supriya, Tailoring layered structure of bismuth-based aurivillius perovskites: recent advances and future aspects. Coord. Chem. Rev. **479**, 215010 (2023)

9. S. Supriya, Recent trends and morphology mechanisms of rare-earth based BiFeO3 nano perovskites with excellent photocatalytic performances. J. Rare Earths **41**, 331–341 (2023)

10. A. Pritam, S. Kumar, V. Shrivastava et al., Probing the effect of LaFeO3 on the structural, electrical, and dielectric properties of Sr0.8Sn0.2Bi2Nb2O9 processed through solid state route method. Mater. Chem. Phys. **316**, 129089 (2024). https://doi.org/10.1016/j.matchemphys.2024.129089

11. S. Supriya, Highly tunable multifunctional rare earth based Bi0.5-xCexNa0.5TiO3 perovskites via site selective doping engineering. Mater. Chem. Phys. (2022). https://doi.org/10.1016/j.matchemphys.2022.126233

12. A. Pritam, V. Shrivastava, Hole/electron transport layers in tin-doped SBLN nano materials for hybrid solar cell applications. J. Mater. Sci. Mater. Electron. **30**, 11054–11062 (2019). https://doi.org/10.1007/s10854-019-01447-1

13. M. Afqir, A. Tachafine, D. Fasquelle et al., Dielectric properties of gadolinium-doped SrBi2Nb2O9 ceramics. J. Mater. Sci. Mater. Electron. **29**, 1289–1297 (2018). https://doi.org/10.1007/s10854-017-8034-8

14. D. Nelis, J.M. Calderon-Moreno, M. Popa et al., Formation and micro-Raman spectroscopic study of Aurivilius and fluorite-type SrBi2Nb2O9 nanocrystallites obtained using an "amorphous citrate" route. J. Eur. Ceram. Soc. **26**, 409–415 (2006). https://doi.org/10.1016/j.jeurceramsoc.2005.07.049

15. S.N. Kumar, P. Kumar, D.K. Agrawal, Structural, dielectric and ferroelectric properties of SBN ceramics synthesized by microwave reactive sintering technique. Ceram. Int. **38**, 5243–5250 (2012). https://doi.org/10.1016/j.ceramint.2012.03.034

16. J. Zhang, G. Wang, F. Gao et al., Influence of Sr/Ba ratio on the dielectric, ferroelectric and pyroelectric properties of strontium barium niobate ceramics. Ceram. Int. **39**, 1971–1976 (2013). https://doi.org/10.1016/j.ceramint.2012.08.048

17. S. Supriya, Effect of sintering temperature and micro structural analysis on sol-gel derived silver bismuth titanate ceramics. Mater. Res. Bull. **96**, 290–295 (2017). https://doi.org/10.1016/j.materresbull.2017.01.018

18. Y. Wu, M.J. Forbess, S. Seraji et al., Doping effect in layer structured SrBi2Nb2O9ferroelectrics. J. Appl. Phys. **90**, 5296–5302 (2001). https://doi.org/10.1063/1.1413236

19. I. Coondoo, N. Panwar, A. Tomar et al., Impedance spectroscopy and conductivity studies in SrBi 2(Ta 1-xW x) 2O9 ferroelectric ceramics. Phys. B Condens. Matter **407**, 4712–4720 (2012). https://doi.org/10.1016/j.physb.2012.09.024

20. K.A. Aly, N.M. Khalil, Y. Algamal, Q.M.A. Saleem, Estimation of lattice strain for zirconia nano-particles based on Williamson–Hall analysis. Mater. Chem. Phys. **193**, 182–188 (2017). https://doi.org/10.1016/j.matchemphys.2017.01.059

21. R. Sivakami, S. Dhanuskodi, R. Karvembu, Estimation of lattice strain in nanocrystalline RuO2 by Williamson–Hall and size-strain plot methods. Spectrochim. Acta A Mol. Biomol. Spectrosc. **152**, 43–50 (2016). https://doi.org/10.1016/j.saa.2015.07.008

22. C.L. Hobday, S. Krause, S.M.J. Rogge et al., Perspectives on the influence of crystal size and morphology on the properties of porous framework materials. Front. Chem. (2021). https://doi.org/10.3389/fchem.2021.772059

23. P. Shunmuga Sundaram, T. Sangeetha, S. Rajakarthihan et al., XRD structural studies on cobalt doped zinc oxide nanoparticles synthesized by coprecipitation method: Williamson–Hall and size-strain plot approaches. Phys. B Condens. Matter **595**, 412342 (2020). https://doi.org/10.1016/j.physb.2020.412342

24. D. Nath, F. Singh, R. Das, X-ray diffraction analysis by Williamson–Hall, Halder–Wagner and size-strain plot methods of CdSe nanoparticles—a comparative study. Mater. Chem. Phys. **239**, 122021 (2020). https://doi.org/10.1016/j.matchemphys.2019.122021

25. T.S. Velayutham, N.I.F. Salim, W.C. Gan, W.H. Abd. Majid, Effect of cerium addition on the microstructure, electrical and relaxor behavior of Sr0.5Ba0.5Nb2O6 ceramics. J. Alloys Compd. **666**, 334–340 (2016). https://doi.org/10.1016/j.jallcom.2015.12.248

26. B. Rajesh Kumar, B. Hymavathi, X-ray peak profile analysis of solid-state sintered alumina doped zinc oxide ceramics by Williamson–Hall and size-strain plot methods. J. Asian Ceram. Soc. **5**, 94–103 (2017). https://doi.org/10.1016/j.jascer.2017.02.001

27. S. Harjo, Y. Tomota, S. Torii, T. Kamiyama, Residual thermal phase stresses in α-γ Fe-Cr-Ni alloys measured by a neutron diffraction time-of-flight method. Mater. Trans. **43**, 1696–1702 (2002). https://doi.org/10.2320/matertrans.43.1696

28. H. Irfan, K.M. Racik, S. Anand, Microstructural evaluation of CoAl2O4 nanoparticles by Williamson–Hall and size–strain plot methods. J. Asian Ceram. Soc. **6**, 54–62 (2018). https://doi.org/10.1080/21870764.2018.1439606

29. S. Devesa, A.P. Rooney, M.P. Graça et al., Williamson-hall analysis in estimation of crystallite size and lattice strain in Bi1.34Fe0.66Nb1.34O6.35 prepared by the sol-gel method. Mater. Sci. Eng. B Solid State Mater. Adv. Technol. **263**, 114830 (2021). https://doi.org/10.1016/j.mseb.2020.114830

30. Z. Yao, H. Li, M. Ma et al., Preparation and electrical properties of (1–x)SrBi2Nb2O9-xBiFeO3 lead-free piezoelectric ceramics. Ceram. Int. **42**, 5391–5396 (2016). https://doi.org/10.1016/j.ceramint.2015.12.075

31. A. Pritam, V. Shrivastava, Microwave derived porosity in tin-doped Sr1-xSnxBi1.95La0.05Nb2O9 nano materials for non-Debye conduction and photocatalytic activity. Phys. B Condens. Matter **593**, 412320 (2020). https://doi.org/10.1016/j.physb.2020.412320

32. P. Mojumdar, R. Shaily, R. Bokolia, Structural properties of strontium bismuth niobate (SrBi2Nb2O9) ferroelectric ceramics. Mater. Today Proc. **47**, 4661–4665 (2021)

33. B. Harihara Venkataraman, T. Fujiwara, T. Komatsu, Synthesis and characterization of rare-earth doped SrBi2Nb2O9 phase in lithium borate based nanocrystallized glasses. J. Solid State Chem. **182**, 1538–1544 (2009). https://doi.org/10.1016/j.jssc.2009.04.004

34. R. Singh, V. Luthra, R.S. Rawat, R.P. Tandon, Structural, dielectric and piezoelectric properties of SrBi2Nb2O9 and Sr0.8Bi2.2Nb2O9 ceramics. Ceram. Int. **41**, 4468–4478 (2015). https://doi.org/10.1016/j.ceramint.2014.11.139

35. R. Singh, M. Gautam, V. Luthra, S. Subramanian, Exploration of the structural, dielectric, ferroelectric, and piezoelectric properties in non-stoichiometric Sr 1−X Bi 2+2X/3 Nb 2 O 9 ceramics. ECS J. Solid State Sci. Technol. **12**, 103005 (2023). https://doi.org/10.1149/2162-8777/acff82

36. G.Z. Liu, C. Wang, H.S. Gu, Lu.H. Bin, Raman scattering study of La-doped SrBi2Nb2O 9 ceramics. J. Phys. D Appl. Phys. **40**, 7817–7820 (2007). https://doi.org/10.1088/0022-3727/40/24/034

37. Z.Y. Zou, X.K. Lan, W.Z. Lu et al., Novel high Curie temperature Ba2ZnSi2O7 ferroelectrics with low-permittivity microwave dielectric properties. Ceram. Int. **42**, 16387–16391 (2016). https://doi.org/10.1016/j.ceramint.2016.07.040

38. Z. Yang, R. Gu, L. Wei, H. Ren, Phase formation, microstructure and dielectric properties of Sr 0.53Ba0.47Nb2-xTaxO6 ceramics. J. Alloys Compd. **504**, 211–216 (2010). https://doi.org/10.1016/j.jallcom.2010.05.093

39. H. Du, Y. Li, H. Li et al., Relaxor behavior of bismuth layer-structured ferroelectric ceramic with m = 2. Solid State Commun. **148**, 357–360 (2008). https://doi.org/10.1016/j.ssc.2008.05.017

40. S.B. Krupanidhi, A. Sharma, A.K. Singh, V. Tuli, *Recent advances in functional materials and devices* (Springer Nature Singapore, Singapore, 2024)

41. A. Tanwar, M. Verma, V. Gupta, K. Sreenivas, A-site substitution effect of strontium on bismuth layered CaBi 4Ti4O15 ceramics on electrical and piezoelectric properties. Mater. Chem. Phys. **130**, 95–103 (2011). https://doi.org/10.1016/j.matchemphys.2011.05.081

42. P. Fang, H. Fan, J. Li et al., The dielectric properties and the relaxation phase transition of copper substituted SrBi2 Nb2 O9 ferroelectric ceramics. Solid State Commun. **149**, 2074–2077 (2009). https://doi.org/10.1016/j.ssc.2009.08.016

43. D. Kajewski, Z. Ujma, K. Szot, M. Pawełczyk, Dielectric properties and phase transition in SrBi2Nb2O9-SrBi2Ta2O9 solid solution. Ceram. Int. **35**, 2351–2355 (2009). https://doi.org/10.1016/j.ceramint.2009.01.013

44. J. Zhang, M. Chao, E. Liang, M. Li, Synthesis and dielectric properties of textured SrBi 2Nb 2O 9 ceramics via laser rapid solidification. J. Alloys Compd. **521**, 150–154 (2012). https://doi.org/10.1016/j.jallcom.2012.01.099

45. F. Rubio-Marcos, J.J. Romero, M.G. Navarro-Rojero, J.F. Fernandez, Effect of ZnO on the structure, microstructure and electrical properties of KNN-modified piezoceramics. J. Eur. Ceram. Soc. **29**, 3045–3052 (2009). https://doi.org/10.1016/j.jeurceramsoc.2009.04.026

46. T.V. Kumar, Dielectric relaxation, ionic conduction and complex impedance studies on NaNo3 fast ion conductor. Int. J. Mater. Sci. Appl. **2**, 173 (2013). https://doi.org/10.11648/j.ijmsa.20130206.12

47. K. Sambasiva Rao, D. Madhava Prasad, P. Murali Krishna, T.S. Latha, Structure, dielectric and impedance properties of barium strontium samarium bismuth niobate ceramic. Ceram. Silik. **52**, 190–200 (2008)

48. B. Harihara Venkataraman, K.B.R. Varma, Frequency-dependent dielectric characteristics of ferroelectric SrBi 2Nb2O9 ceramics. Solid State Ion. **167**, 197–202 (2004). https://doi.org/10.1016/j.ssi.2003.12.020

49. P. Goel, K.L. Yadav, Effect of V+5 doping on structural and dielectric properties of SrBi2Nb2O9 synthesized at low temperature. Phys. B Condens. Matter **382**, 245–251 (2006). https://doi.org/10.1016/j.physb.2006.02.033

50. J. Li, Y. Pu, X. Wang et al., Effect of yttrium doping on the structure, dielectric multiferroic and magnetodielectric properties of Bi5Ti3FeO15 ceramics. J. Mater. Sci. Mater. Electron. **31**, 4345–4353 (2020). https://doi.org/10.1007/s10854-020-02992-w

51. V. Shrivastava, Lattice strain driven dielectric insulation response of Sr1-xCaxBi2Nb2O9 ceramics. J. Adv. Dielectr. **6**, 1650021-1-1650021–6 (2016). https://doi.org/10.1142/S2010135X16500211

52. V. Shrivastava, A. Pritam, A. Joshi, Integrating third phase transition and CO/CO2 contamination in microwave tailored Bi2Mo1−xWxO6 nano materials. J. Mater. Sci. Mater. Electron. **29**, 17388–17396 (2018). https://doi.org/10.1007/s10854-018-9836-z

53. M.P. Dasari, K. Sambasiva Rao, P. Murali Krishna, G. Gopala Krishna, Barium strontium bismuth niobate layered perovskites: dielectric, impedance and electrical modulus characteristics. Acta Phys Pol A **119**, 387–394 (2011). https://doi.org/10.12693/APhysPolA.119.387

54. S. Khasa, P. Singh, S. Sanghi et al., Science and technology structural analysis and dielectric characterization of aurivillius type CaSrBi2Nb2O9 ceramics. J. Integr. Sci. Technol. **2**, 13–21 (2014)

55. K. Sambasiva Rao, D. Madhava Prasad, P. Murali Krishna et al., Impedance and modulus spectroscopy studies on Ba0.1Sr0.81La0.06Bi2Nb2O9 ceramic. Mater. Sci. Eng. B **133**, 141–150 (2006). https://doi.org/10.1016/j.mseb.2006.06.030

56. A. Laha, S. Saha, S.B. Krupanidhi, Analysis of alternating current conduction and impedance spectroscopy study of BaBi2Nb2O9 thin films. Mater. Res. Soc. Symp. Proc. **688**, 241–246 (2002). https://doi.org/10.1557/proc-688-c7.21.1

57. K. Sambasiva Rao, D. Madhava Prasad, P. Murali Krishna et al., Frequency and temperature dependence of electrical properties of barium and gadolinium substituted SrBi2Nb2O9 ceramics. J. Mater. Sci. **42**, 7363–7374 (2007). https://doi.org/10.1007/s10853-007-1555-4

58. B.H. Venkataraman, K.B.R. Varma, Microstructural, dielectric, impedance and electric modulus studies on vanadium—doped and pure strontium bismuth niobate (SrBi2 Nb2O9) ceramics. J. Mater. Sci. Mater. Electron. **16**, 335–344 (2005). https://doi.org/10.1007/s10854-005-1144-8

59. A. Pritam, V. Shrivastava, Deviations from Vegard's law and intense Raman scattering in low-doped Bi2Mo1−xWxO6 (x = 0–10%) ceramics. Phys. Status Solidi B Basic Res. (2020). https://doi.org/10.1002/pssb.201900450

60. P.P.S. Bhadauria, J. Kolte, Impedance and AC conductivity analysis of La-substituted 0.67BiFeO3–0.33BaTiO3 solid solution. Appl. Phys. A Mater. Sci. Process. (2022). https://doi.org/10.1007/s00339-022-05600-2

61. S.K. Patri, P.L. Deepti, R.N.P. Choudhary, B. Behera, Dielectric, impedance and modulus spectroscopy of BaBi2Nb2O9. J. Electroceram. **40**, 338–346 (2018). https://doi.org/10.1007/s10832-018-0135-0

62. D. Dhak, P. Dhak, P. Pramanik, Influence of substitution on dielectric and impedance spectroscopy of Sr 1–x Bi 2 + y Nb 2 O 9 ferroelectric ceramics synthesized by chemical route. Appl. Surf. Sci. **254**, 3078–3092 (2008). https://doi.org/10.1016/j.apsusc.2007.10.097

63. P. Khatri, B. Behera, V. Srinivas, R.N.P. Choudhary, Complex impedance spectroscopic properties of Ba3V 2O8 ceramics. Adv. Mater. Sci. Eng. **2008**, 1–6 (2008). https://doi.org/10.1155/2008/746256